A Study of Base Drag Optimization Using Mass Bleed

Y.K. Lee[1], H.D. Kim[1] and S. Raghunathan[2]

[1]School of Mechanical Engineering
Andong National University, Andong, 760-749, KOREA

[2]School of Aeronautical Engineering
The Queen's University of Belfast, Belfast, NI, BT9 5AG, UK

Abstract

Compressible base flows with mass bleed in a Mach 2.47 freestream have been numerically investigated to find a way to effectively control the base flow for base drag reduction. Axisymmetric, compressible, mass-averaged Navier-Stokes equations are solved using the standard k-ω turbulence model, a fully implicit finite volume scheme and a multi-stage Runge-Kutta scheme. Various base flow characteristics are obtained by the change in the injection parameter, which is defined by the mass flow rate of the bleed jet non-dimensionalized by the product of the base area and freestream mass flux. The results obtained through the present study show that there is an optimum bleed condition that base pressure reaches a maximum value for all afterbody configurations tested, consequently leading to a minimum base drag, when the injection parameter changes.

Introduction

Aerodynamic bodies such as missiles, projectiles, and rockets, generally, undergo significant deterioration of flight performance by drag. For these kinds of flight bodies, especially, the drag in the base region has the most significant contribution to total drag. At transonic speeds, for example, base drag constitutes a major portion up to 50 % of the total drag for typical projectiles at Mach 0.9 [1]. Base drag should, therefore, be considered separately from other pressure drag components. For this reason, the minimization of base drag has been an important issue to date, and considerable effort has been made to find suitable techniques for obtaining low base-drag shell design.

Base drag reduction can be achieved by afterbody boattailing [2], base bleed or base burning [3,4], some vortex suppression devices [5] and their combinations [6]. Such active or passive flow control techniques, basically, manipulate or alter the near-wake flowfield for an increase in base pressure and consequently reduce base drag. These drag control techniques have been applied in somewhat empirical manners to date due to a lack of understanding of viscous-inviscid flow interactions between a near-wake flow and a freestream.
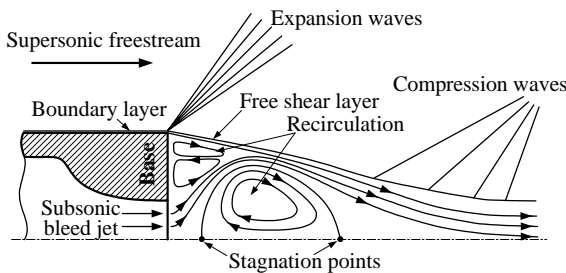
Figure 1. Supersonic base flow with mass bleed.

Figure 1 shows the schematic diagram of the supersonic base flow and afterbody model under consideration in the present computations. The supersonic freestream expands through a

Prandtl-Meyer expansion fan generated at the base corner, and the wall boundary layer developing along the body is separated at the corner and recompressed by compression waves at a certain downstream region. The interaction between two distinct flows inside and outside the separation leads to a free shear layer along the boundary of the flows and recirculating flows inside the separation. In the presence of low mass bleed into the separated region, such flow features can be significantly changed depending on the bleed mass flow rate for a given freestream Mach number and afterbody geometry [7].

According to a computational work conducted by Sahu et al. [1] using thin-layer Navier-Stokes equations, at transonic speeds of Mach 0.9 to 1.2, the use of mass bleed can reduce base drag by 40-80 %. However, the drag does not continuously decrease with increased mass bleed. An experimental study performed by Bourdon and Dutton [8] reported that an optimum condition giving the maximum base pressure was observed at a certain bleed mass flow rate for the given freestream Mach number of about 2.5. This important feature must be replicated with computational results, in order to be considered in aerodynamic design with reliability.

In the present study, a compressible base flow in a supersonic freestream at Mach 2.47 was numerically investigated. Computations have been conducted using axisymmetric mass-averaged Navier-Stokes equations with the standard k-w turbulence model [9]. The results are validated with experimental data [10] and also supported by detailed flow visualization to provide a better understanding of the physics of base flows controlled by a bleed jet.

Numerical Simulations
Afterbody Model
Figure 2 shows the afterbody model used in the present CFD (computational fluid dynamics) analysis, taken from [10] for validation. In the figure, M, p, T are Mach number, pressure and temperature, and subscripts 0, j and ∞ represent a total state, bleed jet and freestream, respectively. The bleed mass flow rate and the Mach number at the orifice exit M_e are calculated by isentropic relations, corresponding to the mass bleed under consideration. Regarding the model dimensions, the diameters of the model and orifice exit are given as R_b and R_e, respectively. The afterbody is taken for computations only up to a length of $3R_b$ from the origin, which lies at the center of the orifice exit.
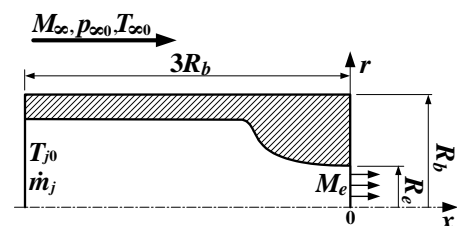
Figure 2. Afterbody model.

M_∞	2.47	T_{j0}	293 K
$p_{\infty 0}$	470 kPa		25.40 mm
p_∞	28.8 kPa	R_b	31.75 mm
$T_{\infty 0}$	300 K		38.15 mm
Re_{unit}	46×10^6 m^{-1}	R_e	12.70 mm

Table 1. Details of CFD model and flow properties.

The details of model geometry and properties given to specify flow conditions are shown in Table 1, where Re_{unit} is the unit Reynolds number of the freestream.

Numerical Methods

The present CFD study adopted a commercial computational code, FLUENT 6, in order to analyze complex flow interactions between a supersonic base flow and a subsonic bleed jet. Axisymmetric compressible mass-averaged Navier-Stokes equations governing the flowfield around an afterbody with mass bleed at the base were solved. The governing equations are discretized spatially and temporally using a fully implicit finite volume scheme and a multi-stage Runge-Kutta scheme [11], respectively in the code. To obtain accurate solutions for the base flow including separation regions, wakes, strong free shear layers and wave systems, suitable turbulence modeling is indispensable. Therefore, preliminary computations were carried out for several turbulence models and wall functions.

Computational Domain and Analysis

Figure 3 shows the grid layout near the afterbody model and brief information of the computational domain used in the current CFD analysis with boundary conditions applied. It has been found that about 50,000 nodes are required to get grid-independent solutions with the computational domain used. Grids were clustered in the regions with large gradient near model surfaces and downstream of the base where the separation of a turbulent boundary layer and wave systems are expected to exist.
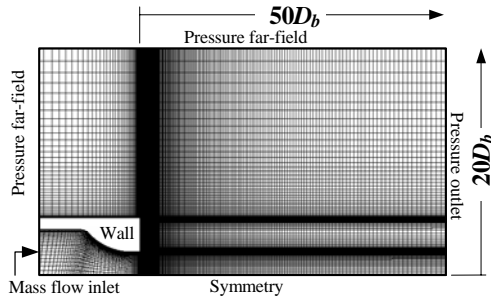
Figure 3. Computational grids.

The computational domain were set up with dimensions of $50D_b$, where D_b is the model diameter, downwards from the base and $20D_b$ upwards from the model axis to ensure freestream conditions and thus to obtain better convergence. Freestream boundaries are identified with a combination of the pressure far-field and pressure outlet conditions as shown in the figure. Preliminary tests showed better convergence could be achieved using the combination rather than the use of the pressure far-field condition at all outer boundaries. To specify the freestream condition, the Mach number and static properties were applied to the boundaries.

Bleed air is injected through an orifice into the near wake region behind the model base. For obtaining various characteristics of mass bleed, the bleed mass flow rate $\dot{m}_j$ applied to the mass flow inlet boundary is changed corresponding to the injection parameter I given as follows.

$$I = \frac{\dot{m}_j}{A_b \rho_\infty U_\infty} \tag{1}$$

where A_b is the base area, and ρ_∞ and U_∞ are the density and velocity of the freestream. With $\dot{m}_j$, total temperature and static pressure are given at the inlet boundary. Adiabatic and no-slip conditions are applied to the wall boundaries, and a symmetry boundary condition is applied to the domain axis. The properties used for the boundary conditions mentioned are given in Table 1.

Regarding testing conditions, I was changed from 0.004 to 0.032 for three base areas tested as the geometry of the orifice and freestream conditions are fixed. The area ratios (A_b/A_e) calculated from R_b values given in Table 1 are 4.00, 6.25 and 9.00, respectively. With a proper grid size and computational domain obtained through preliminary tests, basically, solutions were considered converged when the residuals of mass and momentum equations dropped to 1.0×10^{-4}. The mass imbalance was also checked for flow inlet and outlet boundaries and it is less than $\pm 0.1\%$ for converged solutions.

Results and Discussion

For $I = 0.0038$ and $A_b/A_e = 6.25$, Figure 4 shows grid dependency on the solution given here as axial velocity profiles at $x/R_b = 1.0$ for several grid sizes. The velocity profiles presented have been computed using the standard k-w turbulence model. The radial distance r and the axial velocity U_x are normalized by R_b and U_∞, respectively. The grid size has been tested in a range of about 20,000 to 63,500 nodes. In the figure, the profile inside the back flow region near the axis ($r/R_b = 0.0$) has a relatively significant change for the grid sizes tested. Because grid sizes with more than 45,202 nodes give no more change in the profile, it is considered that 45,202 nodes are enough to have grid independent solutions for the given value of I. For larger I values, in this approach, it has been found that about 50,000 nodes can be used to simulate the flowfields under consideration.
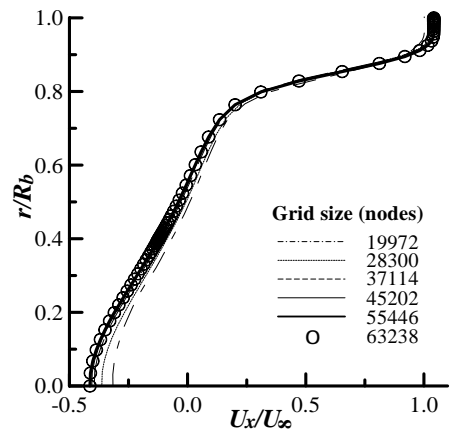
Figure 4. Velocity profiles at $x/R_b = 1.0$ with a change in grid size ($I = 0.0038$ and $A_b/A_e = 6.25$).

With a proper grid size obtained through the approach mentioned above, several turbulence models and wall functions have been tested at $I = 0.0038$ and $A_b/A_e = 6.25$, and base pressure values p_b normalized by p_∞ are given in Table 2. In computations, the grid system was set up to correctly calculate the near-wall flow by checking y+, which was 50 to 200 for the turbulence models with wall functions and less than 1 for the k-w turbulence model. In comparison of computed values and a measured value taken from [10], the standard k-w turbulence model resulted in the closest

prediction of base pressure. The results also indicate that the effect of wall functions on base pressure predictions is insignificant for the geometry and testing conditions used in the present computations.

Turbulence Model		p_b/p_∞
Standard k-ω		0.602
RNG k-ε	SWF	0.569
	NWF	0.572
RSM	SWF	0.571
	NWF	0.580
Experimental, [10]		0.592

Table 2. Base pressure ($I = 0.0038$ and $A_b/A_e = 6.25$).

(a) $I = 0$

(b) $I = 0.0113$ ($A_b/A_e = 6.25$)
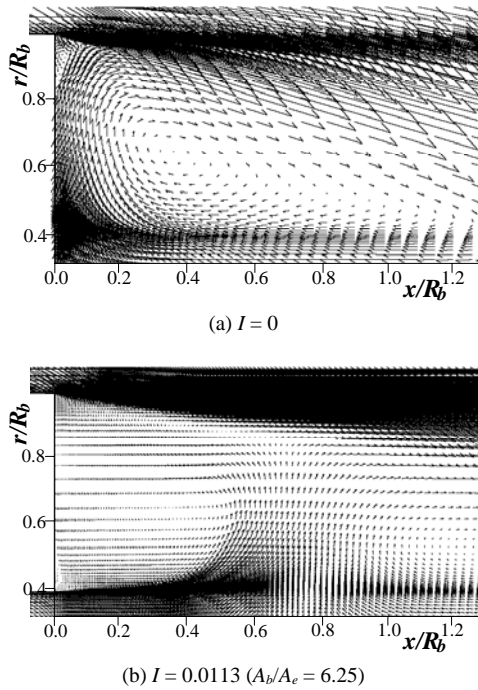
Figure 5. Velocity vectors near the base.

Figure 5 presents mean velocity vectors near the base with and without base bleed. In the figures, axial and normal distances are normalized by R_b. Without base bleed (The whole base region was treated as a wall.), a large and strong recirculating flow is observed. In general, for aerodynamic bodies, base drag rises due to a decrease in base pressure depending on such separation. As mass is injected into the separated region ($I = 0.0113$), the recirculation near the model base becomes significantly weakened.

Base flows visualized computationally at $A_b/A_e = 6.25$ are given in Figure 6 to help an understanding of the detailed flow structures. The computed images (upper half) have been developed by density gradients and these are given with corresponding axial velocity contours valued by U_x/U_∞ (lower half). Inside the separated region, two major recirculation areas are observed near the base and axis. With increased mass bleed, the x-directional directivity of the bleed jet increases, and then the upper recirculation (near the base) becomes stronger and the lower recirculation (near the axis) becomes weaker. These flow characteristics can be apparently shown though axial velocity contours. The lower recirculation moves downstream as I increases. At $I = 0.0226$, the lower separation is almost negligible. Therefore, it is expected that a further increase in I completely moves away the separation from the axis.

(a) $I = 0.0038$

(b) $I = 0.0113$

(c) $I = 0.0226$
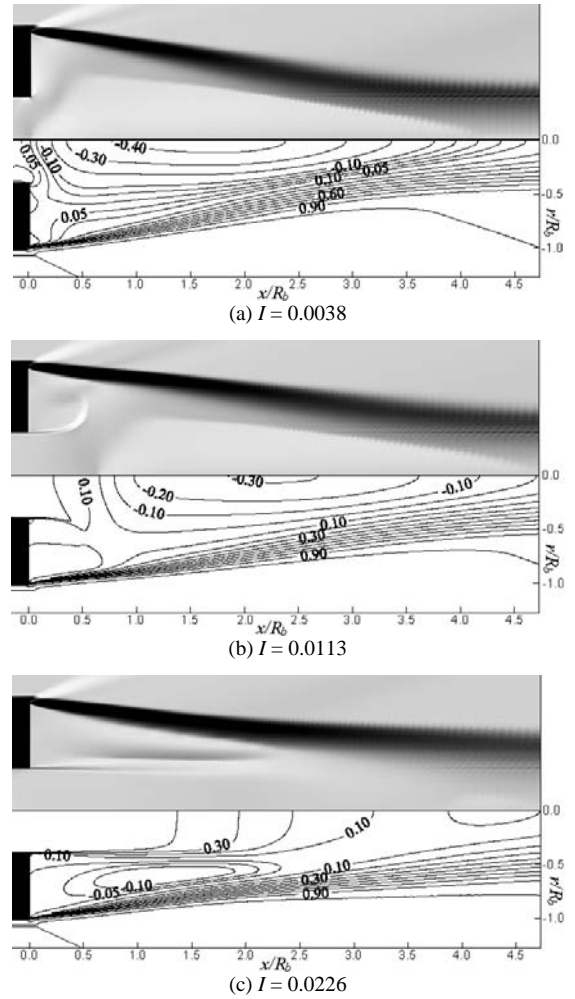
Figure 6. Computed images based on density gradients and U_x/U_∞ contours ($A_b/A_e = 6.25$).

With a change in the injection parameter I, Figure 7 shows base pressure distributions for each base configuration tested. The pressure values estimated along the base are non-dimensionalized by the freestream pressure p_∞. Without base bleed, in general, a large pressure gradient is existent and a very low-pressure region is formed around $r/R_b = 0.65$ due to a strong recirculating flow along the base as observed in Figure 5(a). As I increases, however, such a gradient becomes smaller with an increased pressure level. When I increases over a certain value, consequently, the base pressure level decreases because the recirculation behind the base becomes strong again as shown in Figure 6(c). With an increased area ratio, this behaviour is found at relatively lower I. It can be also found that the base pressure level is higher at a smaller area ratio for given I.

In Figure 8, base pressure obtained through the present CFD method and an experiment [10] are presented with I. The base pressure values shown in the figure are obtained by the production of the area of the base wall and the pressure force acting on the wall. For all base configurations considered, as I increases, base pressure increases up to a maximum value and then decreases. The present computations predict the experimental result properly that the maximum base pressure, leading to minimum base drag, is obtained at $I = 0.0148$ for $A_b/A_e = 6.25$. For a larger area ratio, this optimum condition occurs at relatively lower I and the maximum base pressure which can be achieved by use of mass bleed is lower. From the results discussed in this paper, it is considered that an increase and a
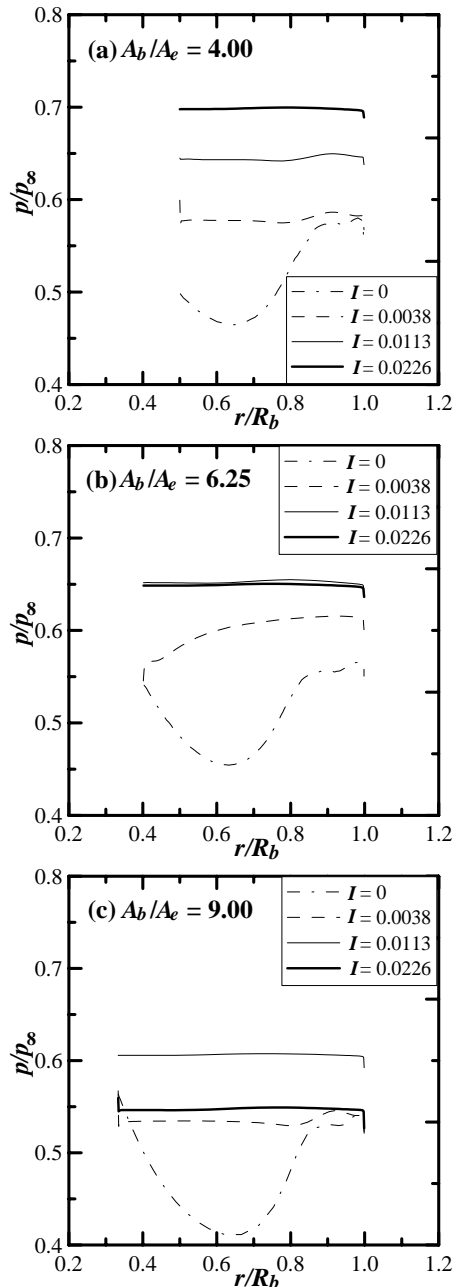
Figure 7. Base pressure distributions with a change in I.
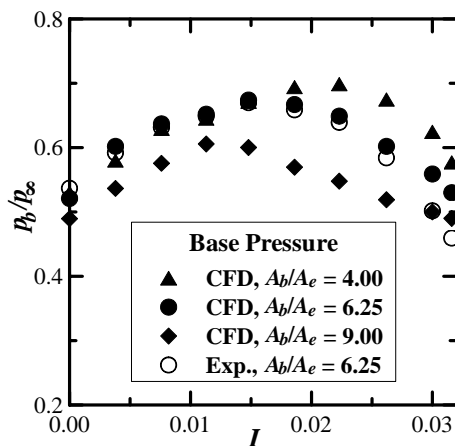
Figure 8. Area-averaged base pressure.

decrease in base pressure as changing mass bleed are decided by

the flow structure characterized by the recirculation regions deformed depending on I, and the base drag control using mass bleed is more effective for smaller A_b/A_e.

Conclusions

For a supersonic freestream of Mach 2.47, the base flow with and without mass bleed generated by an orifice was investigated by CFD as a tool. Axisymmetric, compressible, mass-averaged Navier-Stokes equations were computed using a two-equation turbulence model, standard k-ω, a fully implicit finite volume scheme, and a multi-stage Runge-kutta scheme. The injection parameter and the ratio of base and orifice exit areas were changed to provide various characteristics of subsonic bleed jet flows injected into the severely separated region downstream of the afterbody base.

The results obtained through the present study show that the strong recirculating flows formed near the base and model axis were considerably weakened by use of mass bleed. A change in the mass flow rate of bleed jet led to a significant variation of the flow structure in the separation region behind the base. As the injection parameter increases over a certain value, base pressure distributions became almost uniform. For all afterbody configurations tested, during the mass bleed increase, the average base pressure reached a maximum value. This important feature as shown in a past experimental study could be validated successfully with the present numerical analysis. For a smaller base area, the optimum bleed condition, leading to minimum base drag, occurred at relatively larger mass bleed with better drag control performance.

References

[1] Sahu, J. & Nietubicz, C.J., Navier-Stokes Computations of Projectile Base Flow with and without Mass Injection, *AIAA Journal*, **23**(9), 1985, 1348-1355.

[2] Viswanath, P.R. & Patil, S.R., Effectiveness of Passive Devices for Axisymmetric Base Drag Reduction at Mach 2, *Journal of Spacecraft and Rockets*, **27**(3), 1990, 234-237.

[3] Wood, C.J., Visualisation of an Incompressible Wake with Base Bleed, *Journal of Fluid Mechanics*, **29**(2), 1967, 259-272.

[4] Murthy, S.N.B. & Osborn, J.R., Base Combustion Effects on Base Pressure, Aerodynamics of Base Combustion, *Progress in Astronautics and Aeronautics*, AIAA, **40**, 1976, 307-338.

[5] Nash, J.F., Quincey, V.G. & Callinan, J., Experiments on Two-Dimensional Base Flow at Subsonic and Transonic Speeds, *ARC R&M* 3427, 1966.

[6] Addy, A.L., Thrust-Minus-Drag Optimization by Base Bleed and /or Boattailing, *Journal of Spacecraft and Rockets*, **7**(11), 1360-1362.

[7] Bowman, J.E. & Clayden, W.A., Cylindrical Afterbodies in Supersonic Flow with Gas Ejection, *AIAA Journal*, **5**(8), 1967, 1524-1525.

[8] Bourdon, C.J. & Dutton, J.C., Visualization of a Central Bleed Jet in an Axisymmetric, Compressible Base Flow, *Physics of Fluids*, **15**(2), 2003, 499-510.

[9] Wilcox, D.C., *Turbulence Modeling for CFD*, DCW Industries, Inc., La Canada, California, 1998.

[10] Mathur, T. & Dutton, J.C., Velocity and Turbulence Measurements in a Supersonic Base Flow with Mass Bleed, *AIAA Journal*, **34**(6), 1996, 1153-1159.

[11] Jameson, A., Schmidt, W. & Turkel, E., Numerical Solution of the Euler Equations by Finite Volume Methods Using Runge-Kutta Time-Stepping Schemes, *AIAA paper*, AIAA 81-1259, 1981.